

Nanoscale

Accepted Manuscript



This is an *Accepted Manuscript*, which has been through the Royal Society of Chemistry peer review process and has been accepted for publication.

Accepted Manuscripts are published online shortly after acceptance, before technical editing, formatting and proof reading. Using this free service, authors can make their results available to the community, in citable form, before we publish the edited article. We will replace this *Accepted Manuscript* with the edited and formatted *Advance Article* as soon as it is available.

You can find more information about *Accepted Manuscripts* in the [Information for Authors](#).

Please note that technical editing may introduce minor changes to the text and/or graphics, which may alter content. The journal's standard [Terms & Conditions](#) and the [Ethical guidelines](#) still apply. In no event shall the Royal Society of Chemistry be held responsible for any errors or omissions in this *Accepted Manuscript* or any consequences arising from the use of any information it contains.



Journal Name

ARTICLE

Centimeter-Scale Sub-10-nm Gap Plasmonic Nanorod Array Film as Versatile Platform for Enhancing Light–Matter Interactions

Zhang-Kai Zhou,^{†ac} Jiancai Xue,^{†ac} Zebo Zheng,^{bc} Jiahua Li,^{ac} Yanlin Ke,^{abc} Ying Yu,^d Jun-Bo Han,^d Weiguang Xie,^e Shaozhi Deng,^{abc} Huanjun Chen,^{*abc} Xuehua Wang^{*ac}

Received 00th January 20xx,
Accepted 00th January 20xx

DOI: 10.1039/x0xx00000x

www.rsc.org/

Strongly coupled plasmonic nanostructures with sub-10-nm gaps can enable intense electric field enhancements which greatly benefit the various light–matter interactions. From the point view of practical applications, such nanostructures should be of low-cost, facile fabrication and processing, large-scale with high-yield of the ultrasml gaps, and easy for integration with other functional components. However, nowadays techniques for reliable fabrication of these nanostructures usually involve complex, time-consuming, and expensive lithography procedures, which were limited either in their low-throughput or the small areas obtained. On the other hand, so far most of the studies on the sub-10-nm gap nanostructures mainly focused on the surface-enhanced Raman scattering and high-harmonic generations, while leaving other nonlinear optical properties unexplored. In this work, using scalable process without any lithography procedures, we demonstrated a centimeter-scale ordered plasmonic nanorod array film (PNRAF) with well-defined sub-10-nm interparticle gaps as versatile platform for strongly enhanced light–matter interactions. Specifically, we showed that due to their plasmon-induced localized electromagnetic field enhancements, the Au PNRAF could exhibit extraordinary intrinsic multi-photon avalanche luminescence (MAPL) and nonlinear saturable absorption (SA). Furthermore, the PNRAF can be easily integrated with semiconductor quantum dots (SQDs) as well as wide bandgap semiconductor to strongly enhance their fluorescence and photocurrent response, respectively. Our method can be easily generalized to nanorod array films consisted of other plasmonic metals and even semiconductor materials, which can own multiple functionalities derived from different materials. Overall, the findings in our study have offered a potential strategy for design and fabrication of nanostructures with ultrasml gaps for future photonic and optoelectronic applications.

1 Introduction

Architectures capable of capturing light and modifying the electromagnetic local density of states to enhance light–matter interactions are very important for promoting the performance of various photonic and optoelectronic

devices.^{1–3} Metallic nanostructures sustaining plasmonic resonances have been considered as one of the most promising candidates.⁴ Specifically, gap plasmons which occur in the sub-10-nm gaps between two metal nanostructures are able to focus free-space light into sub-diffraction-limited regions and give rise to strong localized electric field enhancements.^{5,6} Such remarkable property has been utilized for enhancing various light–matter interactions at the nanoscale.^{7–10} Additionally, by carefully reducing the gaps to sub-1-nm scale, exotic plasmon behaviors governed by quantum mechanics can emerge,^{11–13} offering new opportunities for novel quantum plasmonic devices.

A prerequisite for the aforementioned applications is the reliable and reproducible fabrication of coupled metal nanostructures with well-defined and uniform sub-10-nm gaps. In addition, from the application point of view, such nanostructures should be of low-cost, facile fabrication and processing, large-scale with high-yield of the ultrasml gaps, and easy for integration with other functional components, which remain hurdles for nowadays nanofabrication. Currently the most effective approaches for fabrication of such ultrasml gaps usually relies on photo-resist-based lithography procedures,^{14–16} electromigration,¹⁷ or shadow evaporation.^{18,19} These methods were however not favorable

^a State Key Laboratory of Optoelectronic Materials and Technologies.

^b Guangdong Province Key Laboratory of Display Material and Technology.

^c School of Physics and Engineering, Sun Yat-sen University, Guangzhou 510275, China School of Physics and Engineering, Sun Yat-sen University, Guangzhou 510275, China. E-mail: chenjh8@mail.sysu.edu.cn and wangxueh@mail.sysu.edu.cn.

^d Wuhan National High Magnetic Field Center, Huazhong University of Science and Technology, Wuhan 430074, China

^e Department of Physics, Jinan University, Guangzhou 510630, China.

† Electronic Supplementary Information (ESI) available: statistics on the gaps between adjacent nanorods in the Au PNRAF, photograph and additional SEM image of the PNRAF structure, calculated absorption spectra of an individual Au nanorod, decomposition of the reflection spectrum of the Au PNRAF, calculated electric field intensity contour of an individual Au nanorod, large-area AFM topography and s-SNOM image of a typical Au PNRAF, PL spectra of the Au PNRAF, smooth Au film, and pristine AAO template, SEM image and PL spectra of the Au PNRAF consisted of nanorods welded with each other, SEM image showing the Au PNRAF after MAPL measurements, open-aperture Z-scan measurement scheme and additional Z-scan results, PL spectra of SQDs on smooth Au film and silica slide, and photocurrent response of the photodiode consisted of TiO₂ layer sandwiched between smooth Pt and Au films. See DOI: 10.1039/x0xx00000x.

‡ These authors contributed equally.

for practical device design and fabrication either for their cost-intensive and time-consuming procedures or for the low-yields and limited areas of the gaps achieved. Recently, a process combining interference lithography and angular evaporation has been proposed to precisely restrain the gap size below 10 nm with large area,⁶ the delicate control of the metal evaporation angles and thicknesses is nonetheless complex, especially for integration with other functional components. On the other hand, most of the previous studies on the sub-10-nm gap nanostructures mainly focused on the surface-enhanced Raman scattering (SERS) and high-harmonic generations,^{6,14,20–22} while leaving other plasmonic-derived nonlinear optical responses unexplored.

After excitation the plasmons can decay into electron–hole pairs and generate the so-called hot electrons.^{23,24} These energetic hot electrons can thereafter be injected into the adjacent semiconductors, giving rise to their enhanced photocurrent response even under sub-bandgap excitations.²⁵ This property has attracted more and more recent interests and several structures such as nanorod antenna,²⁵ grating structure,²⁶ and particle clusters²⁷ have been proposed. However, to the best of our knowledge, combining the nanostructures of sub-10-nm gaps with semiconductors to increase their photocurrent generation, which designates the direct optoelectronic applications of these gap plasmons, has not yet been studied.

Here, by combining ordered anodic aluminum oxide (AAO) templates with simple sputtering technique, we demonstrated an ordered plasmonic nanorod array film (PNRAF) with well-defined sub-10-nm interparticle gaps which can be facily scaled up to centimeter-scale. By tailoring the morphology of the AAO to form protrusions distributed around each pore, nanorods can be formed by sputtering metal layer onto these protrusions. Consequently, ultrasmall gaps of 5.7 nm can be obtained as the adjacent nanorods were approaching each other due to the increment of their thicknesses. No lithography procedures were involved in this bottom-up method. The ultrasmall gaps can lead to strong plasmon coupling and give rise to collective plasmon modes in the visible range. The strong plasmon-induced electric field enhancements enable the PNRAF as versatile platform for enhancing various light–matter interactions. Specifically, we showed that the PNRAF made up of Au could exhibit extraordinary multi-photon avalanche luminescence (MAPL) with low thresholds. In addition, the Au PNRAF also showed strong nonlinear saturable absorption (SA) behavior with an effective absorption coefficient ($|\beta_{\text{eff}}|$) up to 5.96×10^{-2} cm/W, which was 1 ~ 4 orders of magnitude higher than most of previously reported nanostructured Au films. Besides their intrinsic outstanding nonlinear optical properties, the Au PNRAF can also be utilized as platforms for accelerating the light emission of semiconductor quantum dots (SQDs) and photo-to-current conversion efficiency of optoelectronic devices. In particular, when the Au PNRAF was incorporated into a photodiode, the photocurrent can be remarkably

enhanced in comparison with the conventional device consisted of normal Au film. Finally, we showed that the nanorod array films could be extended to other plasmonic metals and even semiconducting materials, which possessed great potentials as building blocks in future multifunctional and high-performance photonic and optoelectronic devices.

One should note that similar honeycomb-like array structures with spherical- or hemispherical-shape metal nanoparticle units have been reported in previous studies.^{28,29} In comparison with the previous study, we believe that our work has still made several progresses. First, in the previous study honeycomb-like array structures with spherical- or hemispherical-shape metal nanoparticle units were studied, while in our work we focused on nanorod-shaped plasmonic array. In comparison with the spherical nanostructures, nanorods usually exhibit much stronger electric field enhancements when they are arranged into ordered plasmonic arrays due to the collective plasmon coupling of their longitudinal plasmon modes. Such electric field enhancements can strongly benefit various light–matter interactions and thereafter lead to the exotic nonlinear optical properties reported in our study. Secondly, in the previous study, only SERS activity of the plasmonic array was cultivated. In our study, as discussed below, we have systematically explored various optical and optoelectronic processes on the nanorod plasmonic gap array. Last but not the least, the previous study employed relatively complicated multistep process to obtain the nanoparticle array, while in our approach, much easier two-step anodization process was utilized. With our method, nanorod array of size up to centimeter scale can be obtained. Besides, the nanorod array can be facily extended to other plasmonic metals and even semiconducting materials.

2 Results and discussions

2.1 Fabrication of the Au PNRAF

In our study, the ordered Au PNRAF was fabricated using the AAO templates via sputtering technique. In most previous reports the metal nanostructure arrays were prepared directionally along the pores, while in our study the PNRAF was obtained by taking advantage of the specific surface morphology of the AAO templates. Specifically, ordered AAO template was first fabricated using standard procedure, followed by a secondary anodization treatment with higher voltage (Fig. 1a). During the latter anodization, the pores of the AAO were widened with simultaneous dissolution of the alumina. Such dissolution mainly occurred from the inner sidewall of the pores, therefore the alumina connecting two adjacent pores would be removed gradually. In such a manner the dissolution of the alumina portion surrounded by each three adjacent pores was much slower, giving rise to the conical sharp protrusions around each pore (Fig. 1a, Fig. S1†).

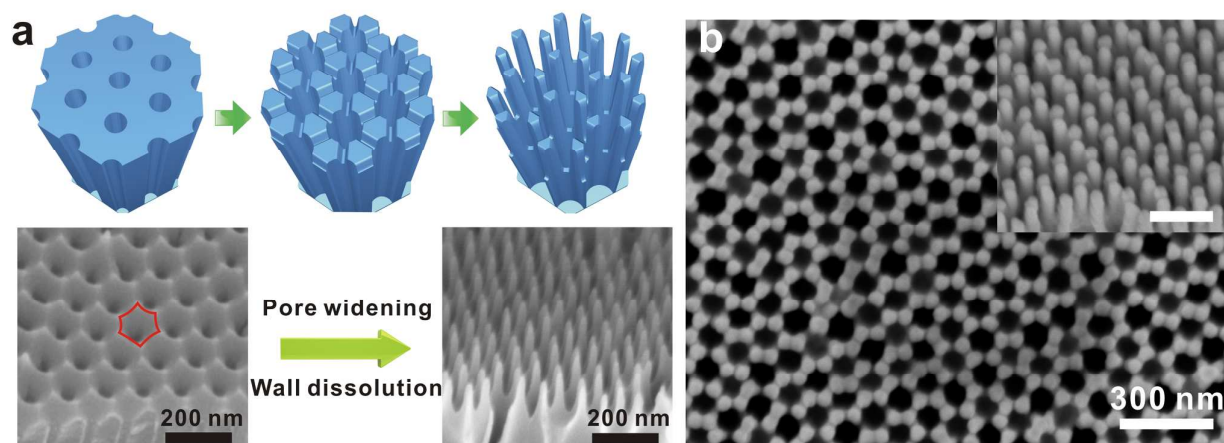


Fig. 1 Preparation of the Au plasmonic nanorod array film (PNRAF) with sub-10-nm gaps. (a) Schematic showing the preparation of the AAO template with conical protrusions (upper) and scanning electron microscope (SEM) images of the as-prepared AAO template and template with conical protrusions (lower). (b) SEM image of the Au PNRAF. Inset is the corresponding tilted side view, with scale bar of 200 nm.

When the metal Au was sputtered onto the AAO templates, the protrusions can act as secondary templates for metal deposition to form nanorod arrays with honey-comb like lattice. As the thickness of the metal layer was increased, the surfaces of the adjacent nanorods will gradually approach towards each other, whereby the voids between them can be narrowed and ultrasmall gaps down to ~ 5.7 nm can be formed (Fig. 1b, Fig. S2[†]). The nanorod array film can be scaled up to centimeter-size with uniform nanorod units by simply utilizing large aluminum plates (Fig. S3a and b in ESI[†]). The diameter and length of the as-prepared nanorods are about 50 and 110 nm, respectively. The diameters of the alumina nanorod cores are about 20 nm (Fig. S1e[†]).

2.2 Plasmonic Properties of the Au PNRAF with Sub-10-nm Gaps

The individual Au nanorod in our current study can exhibit two plasmon resonances (Fig. S3c[†]), with a low-energy mode (longitudinal plasmon mode: LPM) oscillating along the length axis of the nanorods and the other high-energy mode associated with excitation perpendicular to the short axis of the nanorods (transverse plasmon mode: TPM). Due to the ultrasmall gaps, the LPM in an individual nanorod can couple strongly with those of the neighboring nanorods and form collective plasmon modes. The collective plasmon modes can be readily manifested from the reflectance spectra of the Au PNRAF measured with p -polarized light (the electric field has a component parallel to the length axis of the nanorods), which are dominated by broad resonances (Fig. 2a). In contrast to previous studies where collective interactions usually lead to narrow-band plasmon modes,^{30,31} the PNRAF exhibited relatively broad plasmon resonances, which we believed was due to the fluctuations in the sizes and shapes of the nanorods as well as the ultrasmall gaps. The collective nature of the PNRAF plasmon resonance can be further corroborated by the blueshifted resonance peaks with increased excitation angles (Fig. 2a and 2b).³² One should note that under the excitation manner in our study, plasmon coupling should also exist for the TPM because the incidence electric field had component parallel to the short axes of the nanorods. Such coupled TPM

will be submerged into the broad collective LPM mode, which cannot be distinguished from the measured reflectance spectra (Fig. S3d[†]).

Strong electric field enhancements can be induced within the ultrasmall gaps. Fig. 2c gives the simulated electric field distributions under p -polarized excitation at 633 nm for a unit cell containing six Au nanorods with hexagonal arrangements. Notable electric field enhancements rivalling that of an individual nanorod (40 times stronger, Fig. S4[†]) can be observed within the gaps between adjacent nanorods. In addition, relatively smaller electric field enhancements also exist at the center of the unit cell. To experimentally verify such electric field enhancements, apertureless scattering-type scanning near-field optical microscope (s-SNOM) was then utilized for characterizing the near-field optical responses. The measurements were conducted by scanning the sample below an atomic force microscope (AFM), as sketched in Fig. 2d. A typical topography image of the PNRAF is presented in Fig. 2e, showing well-defined honey-comb like lattices composed of uniform nanorods. From the near-field optical image shown in Fig. 2f, regions with distinct optical amplitudes can be found between adjacent nanorods, which confirm the calculated electric field enhancements. Due to the periodicity of the PNRAF, these field enhancements can spread over the region within the laser spot (Fig. S5[†]).

Although the experimentally measured near-field distributions qualitatively agree with the numerical result (Fig. 2c), quantitative agreements are relatively bad. For example, the experimental measurements showed that the near-field intensity in the center of the unit cell was maximal, which was different from the expectations from the simulations. We think that such discrepancy can be understood from two aspects. The first one is the topography artifacts from the s-SNOM measurements. As discussed in previous studies,^{33,34} in s-SNOM operating in tapping mode artifacts with no relation to the optical properties of the sample under the probe can be induced by the variations in the sample surface height. Such effect can be seen more clearly from Fig. S6. When a tip with finite radius scans across the sharp edge of a structure, the AFM feedback loop makes it to retract from the surface, so the

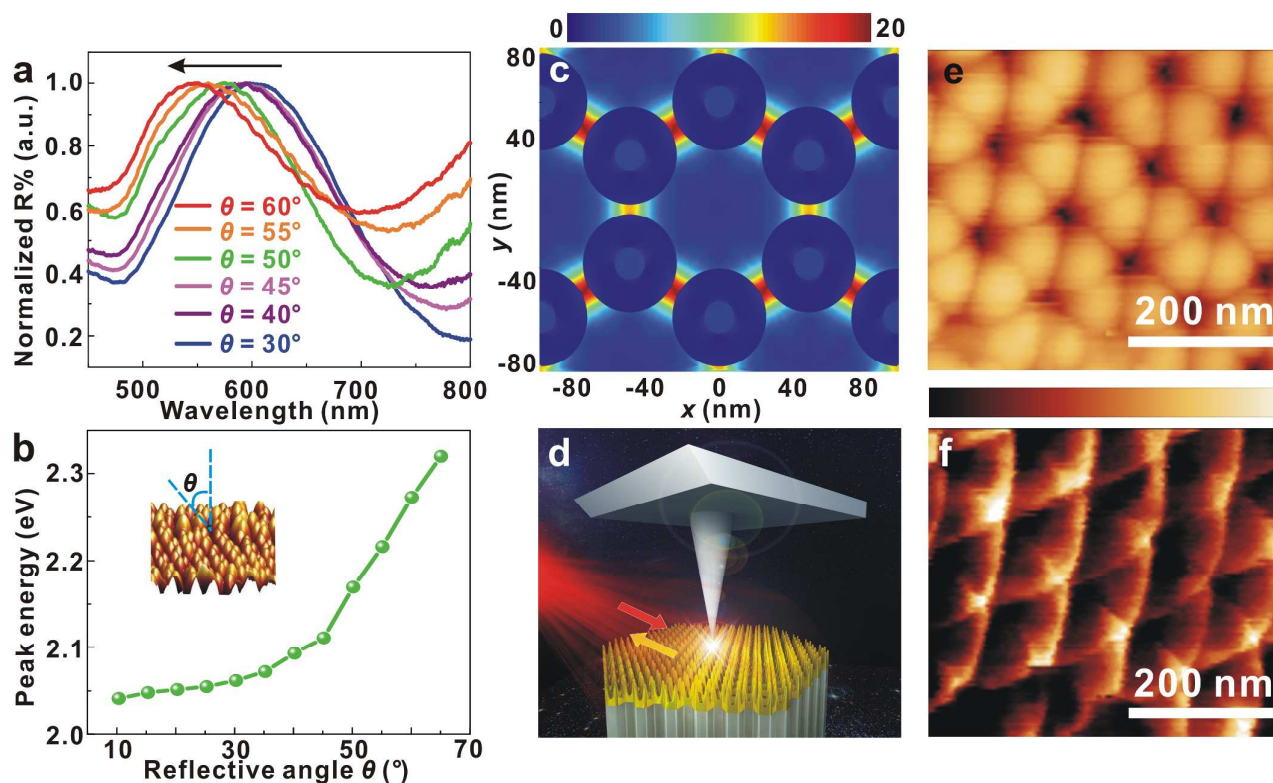


Fig. 2 Plasmonic properties of the Au PNRAF. (a) Normalized reflectance spectra of the PNRAF at different incidence angles. (b) Dependence of the reflectance maxima of the PNRAF on the incidence angles. Inset shows the measurement scheme. (c) Calculated electric field intensity enhancement contour of a unit cell in the PNRAF. The contour is obtained on the cross section 50 nm below the apex of the nanorod. The PNRAF is excited by a *p*-polarized light at an incidence angle of 45° . The excitation wavelength is 633 nm. (d) Schematic showing the scattering-SNOM measurements. (e) AFM topography of a typical Au PNRAF. (f) Optical near-field amplitude at excitation of 633 nm recorded in the same area as that in (e).

distance between tip and region I increases. This reduces the measured near-field signal in region I and leads to artificial larger optical contrast between region I and II. Such topography artifacts become stronger for samples with larger height variations and broader AFM tips. In our study, the height of each nanorod unit is around 130 nm and the radius of the AFM tip is ~ 20 nm. Therefore the topography artifacts will be strong enough to be observed, giving rise to the illusion that the near-field intensity in the center of the unit cell is maximal. However, this illusion can be avoided by using very sharp scanning tips.

Another origin of the discrepancy between the simulation and experimental measurement is their optical excitation manners. In the simulation the nanorod array was excited by a plane wave with *p*-polarization. In the SNOM experiment, the incidence plane wave first coupled with the metal tip and then excited the nanorod array. In such a manner, the excitation felt by the nanorod array was no longer plane wave due to the presence of the metal tip. As result, the measured near field distributions will be not exactly the same with those obtained from the simulations.

2.3 Multi-photon Avalanche Luminescence Properties of the PNRAF

The nonlinear light emission properties of the Au PNRAF with sub-10-nm gaps were studied using femtosecond laser with pulse duration of 100 fs, where the incidence polarization is selected as *p*-polarized. Fig. 3a gives PL spectra of a typical PNRAF under different excitation power with incidence wavelength of 710 nm, which shows emission band ranging from 600 nm to 680 nm. The steep decrease of the emission at wavelength larger than 690 nm is due to the short-pass filter used to block the laser. Such light emission is an intrinsic behavior of the Au PNRAF and can be evidenced via comparing the PL between the PNRAF, smooth Au film, and pristine AAO template (Fig. S7[†]). For the latter two samples no observable PL signal was recorded under the same excitation conditions.

By progressively raising the excitation power, the overall emission spectra of the PNRAF first increased gradually and then underwent a sudden magnification when the excitation power was above a specific threshold around 90 mW (Fig. 3a). To get further insight into the PL properties of the Au PNRAF, the emission intensity at 670 nm was monitored as a function of the excitation power. As expressed from the double-logarithmic scale curves (Fig. 3b), the emission of the Au PNRAF exhibits two clear processes separated by a kink with increasing excitation power. Specifically, when pumped with low power, the emission followed a quadratic dependence with a slope ν ($\nu = \log I_{\text{PL}} / \log I_{\text{exc}}$) of ~ 2 , suggesting a two-photon PL (TPPL) process. On the other hand, the slope increases up to

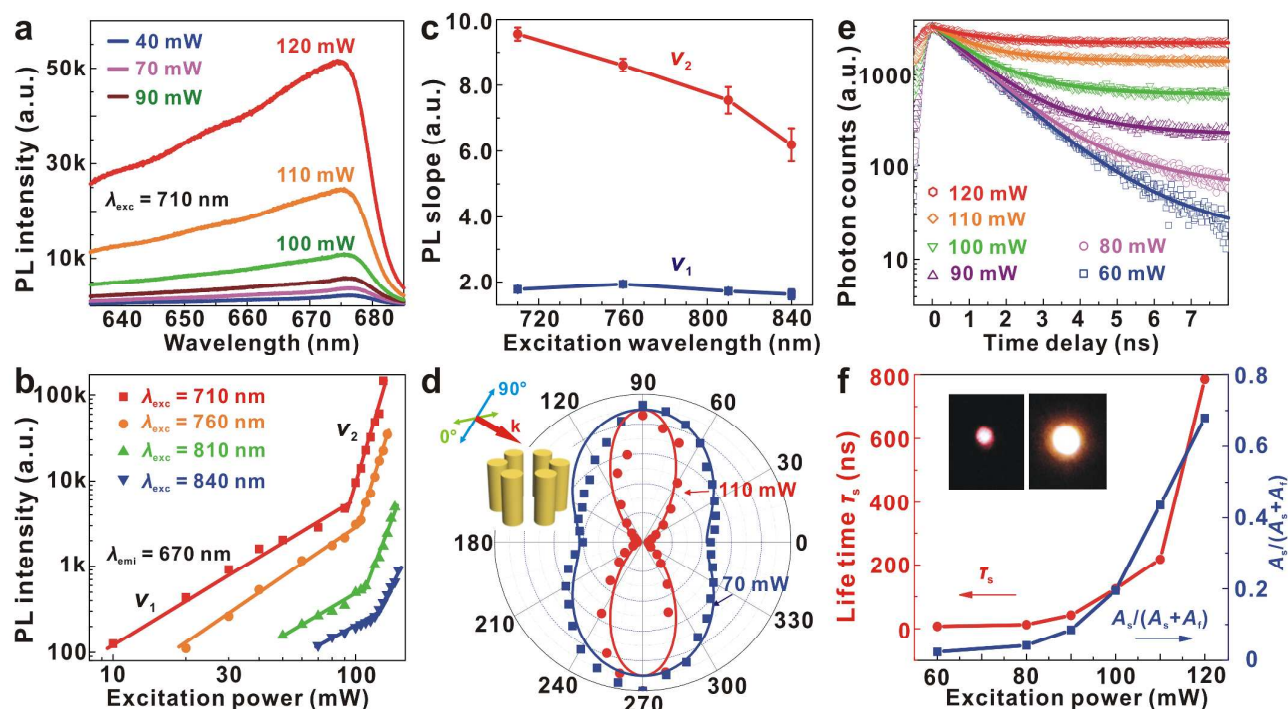


Fig. 3 Nonlinear PL properties of the Au PNRAF. (a) PL spectra from the PNRAF under different excitation power. Femtosecond laser with center wavelength of 710 nm was employed as the excitation source. The sample was excited by a *p*-polarized light at an incidence angle of 45°. (b) Dependence of the PL intensity at 670 nm on the excitation power under different incidence wavelengths. The results are given at the logarithmic scale. The solid lines are linear fits of the experimental data, whereby the slopes v_1 and v_2 can be determined. (c) Dependence of the slopes $v_{1,2}$ on the excitation wavelengths. (d) Excitation polarization dependence of the PL from the PNRAF under two different excitation powers. Inset shows the excitation scheme with varying polarization angle, which is defined as the angle between the excitation polarization and the direction along the short axis of the nanorod. The excitation wavelength is 710 nm and the emission at 670 nm was monitored. (e) Decay traces of the emission from the PNRAF under different excitation power. The solid lines are fitting results using two-exponential decay functions. (f) Dependence of the lifetime and relative intensity ratio of the slow emission process on the excitation power. The solid lines are guides for eyes. The inset gives the real-color images of the emission below (left) and above (right) the excitation threshold.

~ 9.8 for high-power excitation above the threshold, which is a clear evidence for MAPL. To further elucidate the origins of the strong MAPL we then utilized excitations with varied wavelengths to investigate its influence on the PL behaviors. For excitations with different wavelengths, the Au PNRAF exhibited similar nonlinear PL behaviors, with the overall PL intensity significantly increased as the incidence wavelengths were blueshifted. In addition, the slopes for the MAPL process also raised for shorter excitation wavelengths, whereas those for the TPPL process persisted irrespective of the excitation wavelengths (Fig. 3c). Moreover, the intensity thresholds differentiating these two processes decreased from ~ 130 mW to ~ 90 mW as the excitation wavelengths were reduced. These observations can be understood by realizing that both of TPPL and MAPL are nonlinear emission processes and strongly dependent on the electric field intensity. Stronger electric field enhancement will be induced when reducing the excitation wavelengths towards the collective plasmon resonance of the Au PNRAF, whereby more electrons can be excited and then recombined via radiative decay. As a result, strengthened PL intensity, smaller intensity threshold for the MAPL, and higher MAPL slope can be observed for excitation with shorter wavelengths.

The nonlinear PL properties of the Au PNRAF were very sensitive to the polarizations of the excitation. Fig. 3d shows the dependence of the emission intensity at 670 nm on the

excitation polarizations. In these measurements the sample was excited with an incidence angle of 45°. The polarization angle φ is defined as the angles between the excitation polarizations and the direction along the short axis of the nanorod. For excitation with power below the threshold, the TPPL emission exhibits a clear $\sin^2\varphi$ behavior, which is similar to that observed in an individual Au nanorod.³⁵ Such quadratic dependence suggests that it is due to the sequential one-photon process.³⁴ In contrast, for excitation above the threshold, the MAPL intensity obeys a $\sin^6\varphi$ behavior. The maximum emission with $\varphi=90^\circ$ is about 20 times stronger than that excited by *s*-polarized light ($\varphi=0$), indicating the importance of longitudinal plasmon coupling for the MAPL to occur. The $\sin^6\varphi$ dependence is another indication of the multiphoton nature of the emission.

The emission dynamics for the MAPL is much different from that of conventional single-photon emission or TPPL process, as manifested by the transient PL spectra of the Au PNRAF under different excitation powers (Fig. 3e). For low-power excitation, the light emission was governed by the TPPL process and exhibited a nearly single-exponential behavior. However, as the excitation power was progressively increased, the PL from the Au PNRAF evolved into a two-exponential process composed of a fast and a slow process. The dynamic decay of the emission can be well described by the following equation,

$$I_{\text{MAPL}}(\tau) = A_f e^{-\tau/\tau_f} + A_s e^{-\tau/\tau_s} \quad (1)$$

where A_f and A_s are the weights of the fast and slow processes, respectively, and the parameters τ_f and τ_s stand for their corresponding lifetime. The lifetime of the fast process was around 1.2 ns and hardly affected by the excitation intensity. On the contrary, the lifetime for the slow process steadily increased from ~ 7 ns to ~ 780 ns with increasing pumping power (Fig. 3f). Meanwhile, the slow process overwhelmed the fast one and became dominant under strong excitations, which can be seen more clearly from the evolution of its relative intensity ratio shown in Fig. 3f. Under such condition, the emission by the slow process is much brighter with a larger area compared to that of the fast process (Inset of Fig. 3f). These strong and ultraslow decay behaviors strongly verify that the light emission from the Au PNRAF above the excitation threshold is of avalanche nature and not due to the stimulated emission or super radiance.

One interesting observation is that the lifetime of the TPPL process of the Au PNRAF was much longer than those found in previous transient PL measurements (~ 3 ps–2 ns).^{36–40} We ascribe such long lifetime to two mechanisms. The first one is that the light emission of the Au PNRAF is mainly associated with recombinations of electrons close to the Fermi level. During the TPPL process, typical excitation will first initiate the intraband transition of an electron within the sp conduction band of the nanorod. Afterwards, a secondary electron in the d band will absorb another photon and be excited into the sp conduction band. The first electron can relax to states close to the Fermi level by emitting phonons and thereafter recombines with the hole in the d band and radiates. The lifetime is longer for electrons located at states near the Fermi level,⁴¹ the corresponding PL can therefore have a longer lifetime compared to those originated from other excited states. Another reason for the long-lifetime PL is the energy cross relaxation between the nanorods in the PNRAF. Due to the ultraslow nature of the MAPL, the excited electron within a nanorod can easily transfer the energy to the adjacent nanorods before its recombination via the strong electromagnetic coupling. Through such energy cross relaxation process, the effective lifetime of the excited electron can be extended, giving rise to the corresponding long-lifetime emission.⁴² This mechanism can also be employed to explain the even longer lifetime of the MAPL. Besides direct optical excitation, electrons in a nanorod can be excited to the higher states by the energy cross relaxation from adjacent nanorods. In such a manner the population of the states near the Fermi level can be increased suddenly at the pumping threshold. The increase of the high-energy state population will strongly bleach the absorption of the ground state. As a result, the emission will be dramatically slowed down, giving rise to the MAPL with much longer lifetime. The ultraslow nature of the MAPL is consistent with previous theoretical predictions.⁴² Although these two mechanisms can qualitatively explain the possible origins of the dynamics of the TPPL and MAPL from the Au PNRAF, more studies are needed to give quantitative descriptions, which is still underway.

It should be noted that the MAPL behavior as an important plasmon-derived virtue has been observed from nanowire arrays with large aspect ratios.^{43,44} Due to the required strong electric field enhancements, the MAPL only occurred in nanowires with aspect ratios larger than 23. In our study it was surprising that similar MAPL behaviors occurred in Au nanorods with aspect ratio as low as ~ 2 . Small nanorod aspect ratios can benefit the device miniaturization and integration. We attribute such merit to the ultraslow nature of the PNRAF. The small gaps enable strong plasmon coupling and lead to remarkable electric field enhancements, whereby strong nonlinear MAPL can be induced. On the contrary, if the nanorods are welded together by thermal treatment, vanishing of the gaps will eliminate such electric field enhancements, leading to TPPL behavior without avalanche process (Fig. S8†). However, the electric field enhancement within the gaps was double-edged, which could induce thermal damage to the PNRAF by strong laser illumination (Fig. S9†). The morphologies of the nanorods as well as the gaps between adjacent nanorods were modified due to the laser-induced heating effect. Such damage would be harmful for future applications of the PNRAF, whereas it can still be mitigated by coating the nanorods with a thin protecting layer, e.g. Al_2O_3 or SiO_2 layer.

2.4 Nonlinear Saturable Absorption Properties of the Au PNRAF

SA is a very important nonlinear optical property widely utilized in a variety of solid-state passive mode-lock ultrafast laser systems.⁴⁵ The SA is related to the third-order optical nonlinearity and therefore is strongly dependent on the electric field experienced by the operation medium. In this regard, the strong electric field enhancements by the gaps of the Au PNRAF are expected to make it as excellent SA materials. To unveil this merit open-aperture Z-scan technique was applied to study the SA property of the Au PNRAF (Fig. S10a†). In a specific measurement the transmittance of the sample was recorded as the sample moved toward and away from the beam focus. To minimize the possible thermal damage by laser irradiance, we fixed the power of the incidence laser at 30 mW. Furthermore, to reveal the broad operation band of the SA, four laser lines spanning across visible to near infrared regime were utilized.

Fig. 4a gives the normalized transmittance of the Au PNRAF as a function of z , the displacement between the laser focus and sample position, under 510-nm excitation. The transmission exhibited an evident peak at the laser focus due to the reduction of absorption. On the other hand, measurements on pristine AAO template and smooth Au film under the same experimental conditions did not show any SA behaviors, confirming that the nonlinear absorption was indeed originated from the Au PNRAF (Fig. 4a and Fig. S10b–d†). The nonlinear absorption coefficient $|\beta_{\text{eff}}|$, a pivotal parameter characterizing the SA performance, can thereafter be obtained from standard Z-scan theory according to the transmittance trace.^{46,47} As the excitation wavelengths were increased, the $|\beta_{\text{eff}}|$ of the SA first rose and reached maximum at 630 nm, then declined afterwards (Inset of Fig. 4a). The

calculated $|\beta_{\text{eff}}|$ at 630 nm was up to 5.96×10^{-2} cm/W, which to the best of our knowledge was the highest value reported in nanostructured Au thin film systems.^{48–52} Even for the $|\beta_{\text{eff}}|$ measured at 900 nm, it was still larger than most of the previous reported values, suggesting that the Au PNRAF was an excellent broadband SA material. The wavelength dependence of the $|\beta_{\text{eff}}|$ can be easily understood by considering that the observed SA in the Au PNRAF was attributed to bleaching of ground state under strong enough excitation at the focus. The 630-nm excitation was proximal to the collective plasmon band of the Au PNRAF. Therefore bleaching of the ground state will be largest due to the enhanced light absorption when the pump was in resonance with the plasmon band.

2.5 Plasmon-Enhanced Fluorescence of the Au PNRAF

The strong plasmon-induced electric field enhancements within the gaps can be utilized for magnifying the light emission of quantum emitters nearby. Fig. 4b shows the comparison of the emission spectra from SQDs spin-casted onto the Au PNRAF and pristine AAO template, which indicated the significantly enhanced PL (~ 10 times) of the SQDs by the PNRAF. In these measurements, we chose an incidence wavelength of 810 nm in order to exclude the possible interference from the intrinsic light emission of the AAO

template and Au PNRAF. Under such excitation, the Au PNRAF without the SQDs only exhibit weak TPPL (Fig. 3b and Fig. S11†). In addition, under 810-nm excitation the SQDs used in our study exhibited TPPL centered around 665 nm, which was close to the collective plasmon resonance of the Au PNRAF. As a result, the experienced PL enhancement by the SQDs can be maximized. As references we also recorded the PL signals for SQDs deposited onto quartz substrate and smooth Au film, which showed much weaker intensity in comparison with that from the SQDs deposited onto the Au PNRAF (Fig. S11†).

The mechanism for the PL enhancement can be further revealed from the emission dynamics of the SQDs. As shown in Fig. 4c, the SQDs on the Au PNRAF exhibited a much faster PL lifetime (1.3 ns) than those on the pristine AAO template (29.4 ns), indicating that the spontaneous decay of the SQDs was accelerated by the PNRAF due to its strong localized electric field enhancements. Most interestingly, in contrast to many previous results where the accelerated PL followed a two-exponential decay trace,^{53,54} the PL of the SQDs on the Au PNRAF exhibited a single-exponential decay manner. Such observation suggested that nearly all of the SQDs had experienced the electric field enhancements induced by the Au PNRAF. The ~ 30 times emission rate acceleration by the Au PNRAF is among the best results reported using plasmonic structures,⁵⁵ which can be very important for future quantum

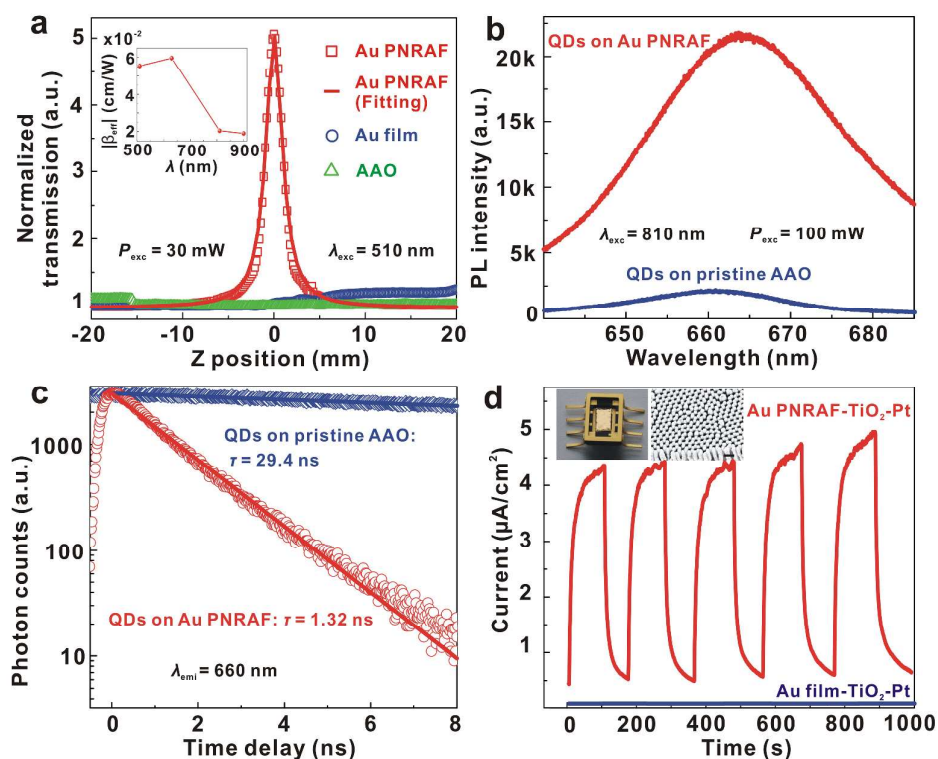


Fig. 4 (a) Open-aperture Z-scan traces of the Au PNRAF, smooth Au film, and pristine AAO template with excitation wavelength of 510 nm. The inset is the dependence of the calculated $|\beta_{\text{eff}}|$ on the excitation wavelengths. (b) and (c) PL and time-resolved PL spectra of SQDs deposited onto the Au PNRAF (red) and pristine AAO template (blue), respectively. The excitation wavelength was 810 nm, with a power of 100 mW. For the transient PL measurements, the PL signal was recorded at 660 nm. (d) Photocurrent responses of a TiO_2 -coated Au PNRAF photodiode (red) and TiO_2 -coated smooth Au film photodiode (blue). The photodiodes were irradiated using a solar simulator with power density of $\sim 100 \text{ mW/cm}^2$. The left inset is photograph of a typical photodiode. The right inset is the titled SEM image of a typical TiO_2 -coated Au PNRAF photodiode. The scale bar is 200 nm.

optics applications dealing with fast signal processing.⁵⁶

2.6 Plasmon-Enhanced Photocurrent Generation of the Au PNRAF

The facile fabrication procedures and large area of the Au PNRAF can greatly benefit its device applications. To demonstrate its potential optoelectronic applications, we incorporated the Au PNRAF into a photodiode and compared the performance to that without such plasmonic structure. In a specific device, a thin Pt layer (10 nm) was first sputtered onto the pristine AAO template as cathode (Fig. S12a†). A 15-nm-thick TiO₂ layer was then deposited onto the cathode by atomic layer deposition (ALD). Finally the Au layer (10 nm) was sputtered onto the TiO₂ layer as the photo anode. The sandwiched structure was then adhered to a chip carrier via wire bonding (Fig. 4d, left inset). The thickness of each layer was chosen to guarantee that the Au layer was conformed to the underlying AAO template, whereby the Au anode preserved the PNRAF morphology (Fig. 4d, right inset). A photodiode with 15-nm TiO₂ sandwiched between two smooth Pt and Au films was also fabricated as reference.

Schottky junctions can be formed between the TiO₂ and Au PNRAF. Under light excitation, the plasmon resonances of the Au PNRAF will generate hot electrons,⁵⁷ which can thereafter diffuse across the Schottky barrier and be injected into the TiO₂ layer.⁵⁸ The presence of the Schottky barrier can prevent the hot electrons from transferred back into the metal. As a result, the photocurrent of the device will be greatly enhanced. Fig. 4d summarizes typical experimental results. When the incidence light on the device from a solar simulator (ABET technologies, Sun 2000) was alternately switched on and off, the photocurrent response of the device with Au PNRAF exhibited clearly contrasted current levels. The dark-state current was due to the applied bias voltage. The measured photocurrent and photocurrent increment turned out to be 4.9 $\mu\text{A}/\text{cm}^2$ and 930~1000%, respectively. For the reference device, the photocurrent was very small (Fig. S12b†). The absolute photocurrent was 53 times smaller than that of the device with PNRAF, while the photocurrent increment was 220 times weaker.

To rule out the possibility that the enhancement of the photocurrent generation is due to increase of the effective active area in the nanostructured device, we then compared the areas of the TiO₂-Au interfaces between the nanostructured and smooth thin film devices. To do so we choose an area of 1 μm^2 . For the Au PNRAF-TiO₂ device, the interface area can be calculated by integrating the TiO₂-Au interface on each nanorod within 1 μm^2 . The nanorods are modelled as cylinders capped with hemispheres. The interface area can thereafter be calculated to be of 2.04 μm^2 . For the smooth film, the interface area is 1 μm^2 . The interface area ratio between these two devices is therefore only 2.04, much smaller than 50. On the other hand, the light source used in the photocurrent measurements is a broad band one covering wavelength range from 350 nm to 1170 nm. Therefore the photocurrent enhancement might also be induced by plasmon-enhanced excitation of the TiO₂ layer. To elucidate

such contribution, we need to compare the photocurrent generation of the device to that under excitation without the UV light. To remove the UV light, we placed a filter which blocks the light below 400 nm in front of the device. By comparing the photocurrent generations between the device with and without such filter (Fig. S13†), one can clearly see that presence of the filter only reduces the photocurrent generation by 7.4%. Such reduction is mainly caused by the additional light absorption from the filter. Therefore the photocurrent contribution from direct excitation of the TiO₂ can be neglected. Overall, we believe that the enhancement of the photocurrent generation in the Au PNRAF-TiO₂ device is indeed due to the plasmonic hot-electron effect.

These results clearly indicated that the Au PNRAF can strongly benefit the photocurrent generation of optoelectronic devices due to its plasmon-induced hot electron injections and large operation area. To the best of our knowledge, this is the first study on possible device applications of the plasmonic structures with sub-10-nm gaps.

2.7 Generalizing the Nanorod Array Film to Other Materials

The studies above have unveiled the exotic plasmon-induced properties of the Au PNRAF that were associated with their sub-10-nm gaps. Future photonic and optoelectronic applications usually require building blocks with multiple functionalities that are derived from different materials. In this regard, we finally show that the nanorod array film with ultrasmall gaps can be easily generalized to other material systems with the same type of AAO template. As shown in Fig. 5a-c, honeycomb-like nanorod array of Ag, Pt, and Al can be obtained by changing the sputtering targets to the respective metals. In addition, by using the ALD method, semiconductor TiO₂ can be well deposited onto the AAO template, forming the TiO₂ nanorod array with similar lattice (Fig. 5d). All of the four nanorod array films exhibit well-defined reflection spectra (Fig. S14†). Such exceptional versatility can distinguish our proposed strategy as excellent fabrication technique for constructing multifunctional metal and semiconductor nanostructure platforms that will meet different application requirements.

3 Conclusions

In conclusion, we have proposed to use delicately-designed AAO templates to fabricate large-area nanorod array films with sub-10-nm gaps. The nanorod can be consisted of various plasmonic metals and semiconductors. For films made up of plasmonic Au nanorods, we have shown that because of the small nanorod gaps down to ~5.7 nm, collective plasmon resonances were observed due to the strong plasmon coupling between adjacent nanorods. The collective plasmon modes can lead to strong electric field enhancements within the gaps, which gave rise to extraordinary nonlinear MAPL and SA behaviors of the Au PNRAF. Furthermore, the strong electric field enhancements can also be utilized for enhancing the light emission intensity of SQDs and photo-to-current conversion

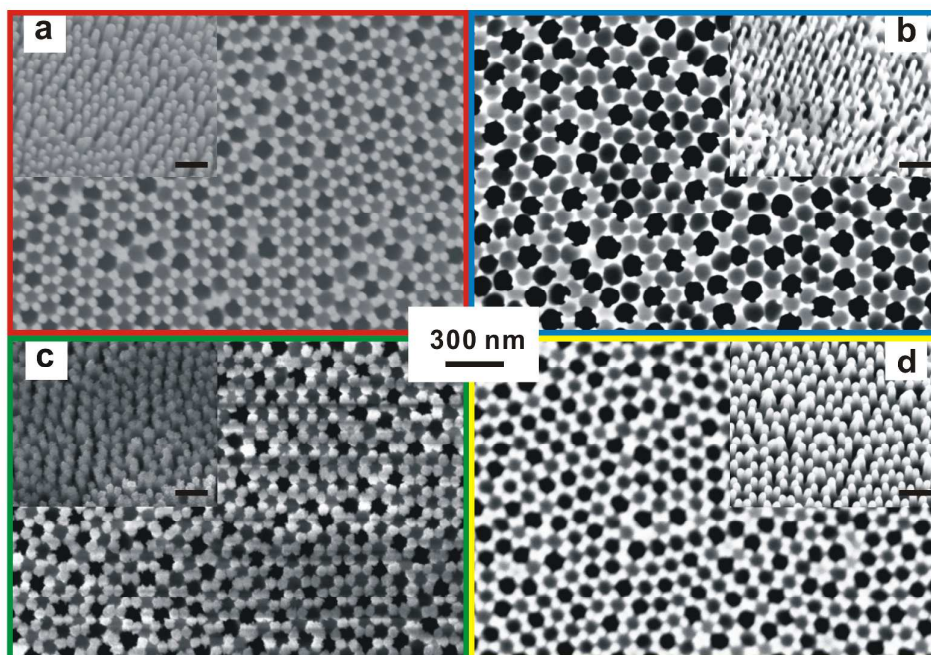


Fig. 5 Morphologies of various nanorod array films with ultrasmall gaps. (a) Ag nanorod array film. (b) Pt nanorod array film. (c) Al nanorod array film. (d) TiO₂ nanorod array film. The insets are respective tilted side views, where the scale bars are 200 nm.

efficiency of photodiodes. We believe that our proposed PNRAF with ultrasmall gaps as well as the related fabrication technique can pave the way for design and building of versatile photonic and optoelectronic devices that will be widely used in signal generation, receiving and processing, energy conversion, and ultrasensitive sensing.

4 Experimental Sections

4.1 Fabrication Details of the PNRAF

The PNRAF were fabricated on the basis of the ordered AAO templates.^{59,60} The templates were prepared using an optimized two-step anodization process. Prior to the anodization the aluminum sheets (purity 99.999%) were degreased in acetone and electropolished under a constant voltage of 16 V for 4 min in a mixture of HClO₄ and C₂H₅OH at 0 °C. In the first anodization step, the treated aluminum sheet was exposed to a H₂C₂O₄ solution (0.3 M) under constant voltage of 40 V at ~4 °C for 3 hours. The alumina layer produced in this process was then removed by wet chemical etching in a mixture of phosphoric acid (0.15 M) and chromic acid (0.60 M) at 60 °C for 1 h. In the second step, the etched alumina sheet was anodized using 10 wt% H₃PO₄. The growth voltage was set to 40 V and lasted for 3 minutes. Thereafter the voltage was quickly raised to 80 V and lasted for another 2 hours. During these processes the preparation temperature was controlled around 15 °C. After the growth of the AAO template, the Au, Ag, Pt, and Al PNRAFs were obtained by sputtering under currents of 60, 60, 5, and 100 mA, respectively (Q150T ES, Quorum). For the growth of TiO₂

nanorod array film, an ALD equipment (Picosun R-series) was employed. For the generation of TiO₂ layer, the prepared AAO template was placed at the center of the ALD chamber with the temperature of 300 °C. Then, pulses of Ti and H₂O vapor were introduced into the chamber, and the pulse duration was 4 s separated by a N₂ purging gas for 8 s. The TiO₂ was slowly grown on the surface of the AAO template, and the thickness can be controlled by tailoring the number of pulse cycles.⁶¹

4.2 Photoluminescence Measurements

All of the photoluminescence measurements in our study were conducted in reflection mode. In a specific measurement, an s-polarized laser was generated by a mode lock Ti: Sapphire laser (MaiTai, Spectra Physics) with a pulse width of ~100 fs and a repetition rate of 79 MHz. The scattering noise was filtered by a band-pass filter. A 150 mm-focal-length lens was used to focus the incident laser onto the sample at an angle of ~45°. The luminescence from the sample was then collected using another lens and transmitted through a long-pass filter before entering the liquid-nitrogen-cooled CCD (SPEC-10, Princeton). Decay traces of the photoluminescence were recorded using a time-correlated single-photon counting system (PicoQuant GmbH). For the SQDs PL measurements, commercial CdSe SQDs (Invitrogen Corporation) were dispersed in polymethyl methacrylate (PMMA) solution (27 nM), and then spin-coated onto the Au PNRAF.

4.3 Z-scan Measurements

A Ti: Sapphire femtosecond laser (Coherent, Mira 900) was applied. The pulse duration and repetition rate were 120 fs

and 76 MHz, respectively. In a specific measurement, after attenuation by a neutral density filter, the laser emission with power of 30 mW was focused onto the sample by a 150 mm-focal-length lens. The sample was then placed onto a moving stage which can be swept along the laser direction ($\pm z$ direction). Two power detectors were used to monitor the laser power (Fig. S10a†). Due to the weak incidence light and the large separation between the sample and power detectors (over 15 cm), the PL of samples can be excluded from the collected signals. For calculating the $|\beta_{\text{eff}}|$, each transmission trace of the Au PNRAF was fitting using the theoretical expression,^{46,47}

$$T = \sum \frac{(-q_0)^m}{(1 + \frac{z^2}{z_0^2})^m (1+m)^2}, \quad (m = 0, 1, 2 \dots)$$

where z_0 is the Rayleigh range and equals to $\pi \omega_0^2 / \lambda$, ω_0 is the Gaussian beam spot radius at the focus ($z=0$), $q_0 = \beta_{\text{eff}} I_0 L_{\text{eff}}$, I_0 is the power intensity of a single pulse at the focal point, which is 0.1074 GW/cm^2 , and L_{eff} is effective thickness of the sample, which in our case is about 15 nm according to the SEM images in Fig. 1.

4.4 Photocurrent Measurements

For fabrication of testing samples in the photocurrent measurements, a thin Pt layer was first sputtered onto the pristine AAO template with 5 mA for 300 s. Then a TiO_2 layer with thickness of 15 nm was deposited by the ALD method with pulse cycle of 150. Finally, Au was sputtered onto the TiO_2 layer with 60 mA for 100 s (Q150T ES, Quorum). For the reference sample, similar sandwich structure was developed except that the AAO template layer was replaced by a silica slide. For photocurrent measurements, the sandwiched structures were first adhered to a carrier chip via wire bonding technique. During the measurements a solar simulator (ABET technologies, Sun 2000) and picoammeter (Keithley 2400) were employed for excitation and recording of the photocurrent, respectively.

4.5 Instrumentation

The reflection spectra were measured on a PerkinElmer Lambda 950 UV-visible-NIR spectrophotometer. SEM imaging was conducted on a Zeiss Auriga-39-34 microscope operating at 5.0 kV. AFM and near-field optical characterizations were conducted using a scattering-type scanning near-field optical microscope (NeaSNOM, Neaspec GmbH). In a specific measurement, an AFM tip coated with metal layer was illuminated using a visible laser with wavelength of 633 nm. The tip is vibrated vertically with frequency around 280 kHz. The backscattered light from the tip was detected using a pseudoheterodyne interferometric manner, where the scattered light was demodulated at fourth harmonic of the tip vibration frequency. By scanning the sample below the tip the optical and morphology images of the sample can be simultaneously obtained.

4.6 Numerical Simulations

The electric field intensity enhancements of the individual Au nanorod and PNRAF were conducted using the commercial software package COMSOL Multiphysics v4.3b in the frequency domain. In the calculations the Au nanorod was modeled as core-shell structure composed of a dielectric Al_2O_3 core with diameter and height of 20 nm and 115 nm, respectively. The thickness of the Au shell was set to 15 nm. The bottom of the nanorod was attached to a dielectric matrix with ordered honeycomb-like air pores inside. The diameter of the air pore was set as 70 nm, and the centre-to-centre distance of two adjacent pores was 95 nm. The refractive index of the Al_2O_3 was 1.76, and the dielectric function of Au was taken from the reported values.⁶² Non-uniform meshes were used. For calculations of the PNRAF we used periodic boundary conditions in the x and y directions while perfectly matched layers (PMLs) in the z direction. The used unit cell was taken as $200 \text{ nm} \times 173 \text{ nm} \times 3500 \text{ nm}$. For calculating the electric field enhancement of the individual Au nanorod, PMLs were utilized in all directions.

Acknowledgements

This work was supported in part by National Natural Science Foundation of China (11204385, 11204089, 51202300, 11474364, 51290271), National Basic Research Program of China (2010CB923200, 2011TS105), the Guangdong Natural Science Foundation (2014A030313140), the Doctoral Fund of Ministry of Education of China (Grant No.: 20120171120012), the Program for Changjiang Scholars and Innovative Research Team in University (Grant No.: IRT13042), and the Fundamental Research Funds for the Central Universities.

Notes and references

- 1 E. Ozbay, *Science*, 2006, **311**, 189–193.
- 2 W. Lu and C. Lieber, *Nat. Mater.*, 2007, **6**, 841–850.
- 3 T. Byrnes, N. Y. Kim and Y. Yamamoto, *Nat. Phys.*, 2014, **10**, 803–813.
- 4 W. L. Barnes, A. Dereux and T. W. Ebbesen, *Nature*, 2003, **424**, 824–830.
- 5 J. A. Schuller, E. S. Barnard, W. Cai, Y. C. Jun, J. S. White and M. L. Brongersma, *Nat. Mater.*, 2010, **9**, 193–205.
- 6 T. Siegfried, Y. Ekinici, O. J. F. Martin and H. Sig, *Nano Lett.*, 2013, **13**, 5449–5453.
- 7 N. C. Lindquist, P. Nagpal, K. M. McPeak, D. J. Norris and S. H. Oh, *Rep. Prog. Phys.*, 2012, **75**, 036501.
- 8 C. Ciraci, R. T. Hill, J. J. Mock, Y. Urzhumov, A. I. Fernández-Domínguez, S. A. Maier, J. B. Pendry, A. Chilkoti and D. R. Smith, *Science*, 2012, **337**, 1072–1074.
- 9 N. A. Hatab, C. H. Hsueh, A. L. Gaddis, S. T. Retterer, J. H. Li, G. Eres, Z. Y. Zhang and B. H. Gu, *Nano Lett.*, 2010, **10**, 4952–4955.
- 10 D. K. Lim, K. S. Jeon, M. H. Kim, J. M. Nam and Y. D. Suh, *Nat. Mater.*, 2010, **9**, 60–67.
- 11 K. J. Savage, M. M. Hawkeye, R. Esteban, A. G. Borisov, J. Aizpurua and J. J. Baumberg, *Nature*, 2012, **491**, 574–577.
- 12 R. Esteban, A. G. Borisov, P. Nordlander and J. Aizpuruz, *Nat. Commun.* 2012, **3**, 825.

- 13 J. Zuloaga, E. Prodan and P. Nordlander, *Nano Lett.*, 2009, **9**, 887–891.
- 14 H. G. Duan, H. L. Hu, K. Kumar, Z. X. Shen and J. K. W. Yang, *ACS Nano*, 2011, **5**, 7593–7600.
- 15 H. G. Duan, A. I. Fernández-Domínguez, M. Bosman, S. A. Maier and J. K. W. Yang, *Nano Lett.*, 2012, **12**, 1683–1689.
- 16 H. G. Duan, V. R. Manfrinato, J. K. W. Yang, D. Winston, B. M. Cord and K. K. Berggren, *J. Vac. Sci. Technol. B*, 2010, **28**, H11–H17.
- 17 D. R. Ward, F. Huser, F. Pauly, J. C. Cuevas and D. Natelson, *Nat. Nanotechnol.*, 2010, **5**, 732–736.
- 18 R. Stosch, F. Yaghobian, T. Weimann, R. J. C. Brown, M. J. T. Milton and B. Güttler, *Nanotechnology*, 2011, **22**, 105303.
- 19 J. Theiss, P. Pavaskar, P. M. Echtenach, R. E. Muller and S. B. Cronin, *Nano Lett.*, 2010, **10**, 2749–2754.
- 20 M. Chirumamilla, A. Toma, A. Gopalakrishnan, G. Das, R. P. Zaccaria, R. Krahne, E. Rondanina, M. Leoncini, C. Liberale, F. D. Angelis and E. D. Fabrizio, *Adv. Mater.*, 2014, **26**, 2353–2358.
- 21 H. Im, K. C. Bantz, N. C. Lindquist, C. L. Haynes and S. H. Oh, *Nano Lett.* 2010, **10**, 2231–2236.
- 22 H. Kollmann, X. J. Piao, M. Esmann, S. F. Becker, D. C. Hou, C. Huynh, L. O. Kautschor, G. Bösker, H. Vieker, A. Beyer, A. Götzhäuser, N. K. Park, R. Vogelgesang, M. Silies and C. Lienau, *Nano Lett.*, 2014, **14**, 4778–4784.
- 23 M. L. Brongersma, N. J. Halas and P. Nordlander, *Nat. Nanotechnol.*, 2015, **10**, 25–34.
- 24 C. Clavero, *Nat. Photonics*, 2014, **8**, 95–103.
- 25 M. W. Knight, H. Sobhani, P. Nordlander and N. J. Halas, *Science*, 2011, **332**, 702–704.
- 26 A. Sobhani, M. W. Knight, Y. M. Wang, B. Zheng, N. S. King, L. V. Brown, Z. Y. Fang, P. Nordlander and N. J. Halas, *Nat. Commun.* 2013, **4**, 1643.
- 27 Z. Y. Fang, Z. Liu, Y. M. Wang, P. M. Ajayan, P. Nordlander and N. J. Halas, *Nano Lett.*, 2012, **12**, 3808–3813.
- 28 P. Nielsen, O. Albrektsen, S. Hassing and P. Morgen, *J. Phys. Chem C*, 2010, **114**, 3459–3465.
- 29 K. Sun, G. Meng, Q. Huang, Z. Zhao, C. Zhu, Z. Huang, Y. Qian, X. Wang and X. Hu, *J. Mater. Chem. C*, 2013, **1**, 5015–5022.
- 30 A. V. Kabashin, P. Evan, S. Pastkovsky, W. Hendren, G. A. Wurtz, R. Atkinson, R. Pollard, V. A. Podolskiy and A. V. Zayats, *Nat. Mater.*, 2009, **8**, 867–871.
- 31 G. A. Wurtz, R. Pollard, W. Hendren, G. P. Wiederrecht, D. J. Gosztola, V. A. Podolskiy and A. V. Zayats, *Nat. Nanotechnol.*, 2011, **6**, 107–111.
- 32 P. R. Evans, R. Kulloch, W. R. Hendren, R. Atkinson, R. J. Pollard and L. M. Eng, *Adv. Funct. Mater.*, 2008, **18**, 1075–1079.
- 33 T. Taubner, R. Hillenbrand and F. Keilmann, *J. Microsc.*, 2003, **210**, 311–314.
- 34 L. Billot, M. L. de la Chapelle, D. Barchiesi, S.-H. Chang, S. K. Gray, J. A. Rogers, A. Bouhelier, P.-M. Adam, J.-L. Bijeon, G. P. Wiederrecht, R. Bachelot and P. Royer, *Appl. Phys. Lett.*, 2006, **89**, 023105.
- 35 A. Bouhelier, R. Bachelot, G. Lerondel, S. Kostcheev, P. Royer and G. P. Wiederrecht, *Phys. Rev. Lett.*, 2005, **95**, 267405.
- 36 K. Imura, T. Naghara and H. Okamoto, *J. Phys. Chem. B*, 2005, **109**, 13214–13220.
- 37 S. Link, C. Burda, M. B. Mohamed, B. Nikoobakht and M. A. El-Sayed, *Phys. Rev. B*, 2000, **61**, 6086–6090.
- 38 S. Link, C. Burda, Z. L. Wang and M. A. El-Sayed, *J. Chem. Phys.*, 1999, **111**, 1255–1264.
- 39 T. T. Zhao, X. F. Jiang, N. Y. Gao, S. Li, N. Zhou, R. Z. Ma and Q. H. Xu, *J. Phys. Chem B*, 2013, **117**, 15576–15583.
- 40 X. F. Jiang, Y. L. Pan, C. F. Jiang, T. T. Zhao, P. Y. Yuan, T. Venkatesan and Q. H. Xu, *J. Phys. Chem Lett.*, 2013, **4**, 1634–1638.
- 41 C. Kittel, *Introduction to Solid State Physics*, John Wiley & Sons: New York, 1986.
- 42 Q. Shu and S. C. Rand, *Phys. Rev. B*, 1997, **55**, 8776–8783.
- 43 Q. Q. Wang, J. B. Han, D. L. Guo, S. Xiao, Y. B. Han, H. M. Gong and X. W. Zou, *Nano Lett.*, 2007, **7**, 723–728.
- 44 H. M. Gong, Z. K. Zhou, S. Xiao, X. R. Su and Q. Q. Wang, *Plasmonics*, 2008, **3**, 59–64.
- 45 A. Martinez and Z. Sun, *Nat. Photonics*, 2013, **7**, 842–846.
- 46 Z. Chen, H. Dai, J. Liu, Z. Li, Z. K. Zhou and J. B. Han, *Opt. Express*, 2013, **21**, 17568–17575.
- 47 Z. K. Zhou, M. Li, X. R. Su, Y. Y. Zhai, H. Song, J. B. Han and Z. H. Hao, *Phys. Stat. Sol. a*, 2008, **205**, 345–349.
- 48 Y. Yu, S. S. Fan, X. Wang, Z. W. Ma, H. W. Dai and J. B. Han, *Mater. Lett.*, 2014, **134**, 233–236.
- 49 D. D. Smith, Y. Yoon, R. W. Boyd, J. K. Campbell, L. A. Baker, R. M. Crooks and M. George, *J. Appl. Phys.*, 1999, **86**, 6200–6205.
- 50 N. Rotenberg, A. D. Bristow, M. Pfeiffer, M. Betz and H. M. Van Driel, *Phys. Rev. B*, 2007, **75**, 155426.
- 51 K. Wang, H. Long, M. Fu, G. Yang and P. X. Lu, *Opt. Express*, 2010, **18**, 13874–13879.
- 52 E. Xenogiannopoulou, K. Iliopoulos, S. Couris, T. Karakouz, A. Vaskevich and I. Rubinstein, *Adv. Funct. Mater.*, 2008, **18**, 1281–1289.
- 53 J. H. Song, T. Atay, S. Shi, H. Urabe and A. V. Nurmikko, *Nano Lett.*, 2005, **5**, 1557–1561.
- 54 K. Munechika, Y. Chen, A. F. Tillack, A. P. Kulkarni, I. J. L. Plante, A. M. Munro and D. S. Ginger, *Nano Lett.*, 2010, **10**, 2598–2603.
- 55 A. Kinkhabwala, Z. Yu, S. Fan, Y. Avlasevich, K. Müllen and W. E. Moerner, *Nat. Photonics*, 2009, **3**, 654–657.
- 56 C. Sauvan, J. P. Hugonin, I. S. Maksymov and P. Lalanne, *Phys. Rev. Lett.*, 2013, **110**, 237401.
- 57 Y. Tian and T. Tsumura, *J. Am. Chem. Soc.*, 2005, **127**, 7632–7637.
- 58 Y. K. Lee, C. H. Jung, J. Park, H. Seo, G. A. Somorjai and J. Y. Park, *Nano Lett.*, 2011, **11**, 4251–4255.
- 59 Z. K. Zhou, D. Y. Lei, J. M. Liu, X. Liu, J. C. Xue, Q. Z. Zhu, H. J. Chen, T. R. Liu, Y. Y. Li, H. B. Zhang and X. H. Wang, *Adv. Opt. Mater.*, 2014, **2**, 56–64.
- 60 C. R. Martin, *Science*, 1994, **266**, 1961–1966.
- 61 H. Xu, J. Liu, X. Duan, J. Li, J. Xue, X. Sun, Y. Cai, Z. K. Zhou and X. Wang, *Opt. Mater. Express*, 2014, **4**, 2586–2594.
- 62 P. B. Johnson and R. W. Christy, *Phys. Rev. B*, 1972, **6**, 4370–4379.